
This manuscript has been submitted for publication in *Ocean Modelling*. Please note that, the manuscript is currently under review and has yet to be formally accepted for publication. Subsequent versions of this manuscript may have slightly different content. If accepted, the final version of this manuscript will be available via the 'Peer-reviewed Publication DOI' link.

Cautionary tales from the mesoscale eddy diffusivity tensor

Takaya Uchida, COAPS (takaya.uchida@univ-grenoble-alpes.fr)

Dhruv Balwada, LDEO (dhruvbalwada@gmail.com)

Quentin Jamet, INRIA (quentin.jamet@inria.fr)

William K. Dewar, FSU (wdewar@fsu.edu)

Bruno Deremble, CNRS (bruno.deremble@univ-grenoble-alpes.fr)

Thierry Penduff, CNRS (thierry.PENDUFF@cnrs.fr)

Julien Le Sommer, CNRS (julien.Lesommer@univ-grenoble-alpes.fr)

Cautionary tales from the mesoscale eddy diffusivity tensor

Takaya Uchida^{a,b,*}, Dhruv Balwada^c, Quentin Jamet^d, William K. Dewar^{b,e},
Bruno Deremble^b, Thierry Penduff^b, Julien Le Sommer^b

^a*Center for Ocean-Atmospheric Prediction Studies, Florida State University, Tallahassee, Florida, USA*

^b*Université Grenoble Alpes, CNRS, IRD, Grenoble-INP, Institut des Géosciences de l'Environnement, Grenoble, France*

^c*Lamont Doherty Earth Observatory, Columbia University in the City of New York, Palisades, New York, USA*

^d*INRIA, ODYSSEY group, Ifremer, Plouzané, France*

^e*Department of Earth, Ocean and Atmospheric Science, Florida State University, Tallahassee, Florida, USA*

Abstract

The anisotropic mesoscale eddy diffusivity tensor is diagnosed using passive tracers advected in both an idealized 101-member mesoscale-resolving quasi-geostrophic (QG) double-gyre ensemble, and a realistic 24-member eddy (1/12°) ensemble of the North Atlantic. We assert that the Reynolds decomposition along the ensemble dimension, rather than the spatial or temporal dimension, allows us to capture the intrinsic spatiotemporal variability of the mean flow and eddies. The tensor exhibits good performance in reconstructing the eddy fluxes of passive tracers, here defined as fluctuations about the ensemble thickness-weighted averaged (TWA) mean. However, the inability of the tensor to reconstruct eddy fluxes of QG potential vorticity, which encapsulates the eddy-mean flow interaction, and other active tracers raises the question, to what extent the diagnosed tensor can be applied to inform the parametrization of mesoscale dynamics.

Keywords: Ensemble simulation, mesoscale eddy, eddy diffusivity, thickness-weighted average

*Email: takaya.uchida@univ-grenoble-alpes.fr

1. Introduction

In the field of computational oceanography, there is never enough computational power to resolve all the spatiotemporal scales of interest, spanning from on the order of $O(1\text{ m})$ to $O(1000\text{ km})$ and seconds to centuries respectively. Nevertheless, with the continuous increase in computational power, global fully-coupled ocean simulations with spatial resolution of $O(10\text{ km})$ have emerged (e.g. Small et al., 2014; Uchida et al., 2017; Chang et al., 2020). This new generation of ocean simulations have improved the representation of oceanic processes, e.g. the oceanic jets in the separated Gulf Stream and Atlantic Circumpolar Current, and the global oceanic heat transport estimates match better with observations (Griffies et al., 2015; Chassignet et al., 2020). Nevertheless, forced ocean simulations with even higher model resolution have shown that even at $O(10\text{ km})$, mesoscale eddies and their feedback onto the jets are not sufficiently resolved (Chassignet and Xu, 2021; Uchida et al., 2019, 2022c; Hewitt et al., 2022).

In order to overcome the insufficient representation of the eddies and their variability, there has been a growing field of research on how to parametrize the effects of eddies in simulations at the grey zone resolution, when the eddy variability is partially resolved. A particular example is energy-backscattering (E-B) parametrizations, where one re-injects the unresolved missing dynamics back into the resolved flow (e.g. Jansen et al., 2019; Bachman, 2019; Guillaumin and Zanna, 2021; Uchida et al., 2022a, and references therein). In this study, we examine the possibility of capturing the backscattering within the framework of eddy diffusivities where one attempts to represent the sub-grid fluxes of tracers via the gradient flux of the resolved tracer fields. In doing so, we utilized two sets of ensemble simulations: an idealized 101-member quasi-geostrophic (QG) double-gyre ensemble at mesoscale-resolving resolution and a realistic eddying ($1/12^\circ$) 24-member North Atlantic (NA) ensemble.

In the parametrization literature, it is common to frame the eddies as the sub-grid variability and mean flow as the resolved flow under limited model resolution, where the eddy and mean are defined using a Reynold's decomposition (Bachman et al., 2015). The assumption, and hope, is that the reduced variability in the mean flow, diagnosed by filtering a high-resolution or observed flow field, would mimic the partially resolved variability at coarser model resolution. In a seminal paper, Young (2012) demonstrated that when the equations of oceanic motions are Reynold's decomposed via a thickness

38 weighted averaging, the net effect of the eddies onto the mean flow can be
39 represented in terms of eddy Ertel’s potential vorticity (PV) fluxes on the
40 thickness-weighted averaged (TWA) mean momentum equations. With this
41 interpretation, the goal of the E-B parametrization problem is to represent
42 the eddy QG or Ertel’s PV fluxes in terms of the mean fields (Young, 2012;
43 Marshall et al., 2012; Vallis, 2017). In this study we address the question:
44 Can the eddy fluxes be expressed in terms of a tensor diffusion model, where
45 the eddy flux is related to the local gradient through a diffusion tensor? Also,
46 is the diffusion tensor for active tracers (e.g. PV) similar to a diffusion ten-
47 sor for passive tracers? Our approach is to diagnose the diffusivities using
48 passive tracers outputs and then to examine whether this can be applied
49 to reconstruct eddy fluxes of active tracers. The interchangeability between
50 passive (in the sense that they do not affect the dynamics) and active tracers
51 such as PV has its history in that the governing equations for the two take
52 a similar form of an advective-diffusive equation (with the caveat that PV is
53 directly linked to the momentum and buoyancy while passive tracers are not;
54 Killworth, 1997; Wilson and Williams, 2006; Eden and Greatbatch, 2008).

55 For practical reasons, a time or spatial mean has often been employed to
56 Reynold’s decompose the flow into its eddy and mean in diagnostic studies.
57 However, this comes with its own issues regarding interpretation. For a tem-
58 porally varying system, such as the real ocean, defining the mean flow via a
59 time mean conflates intrinsic variability of the ocean with the variability in
60 the atmospheric forcing (Aiki and Richards, 2008; Fedele et al., 2021; Uchida
61 et al., 2022b). There are also issues surrounding how to choose the filtering
62 scale, and what model resolution, if any, the scale corresponds to (Bachman
63 et al., 2015). An alternative approach is to define the mean via an ensemble
64 mean, where the intrinsic variability is expressed as eddies and the oceanic re-
65 sponse to atmospheric forcing as the mean (S erazin et al., 2018; Leroux et al.,
66 2018; Uchida et al., 2022b). Taking the ensemble outputs, we, therefore, de-
67 fine the eddy-mean flow decomposition along the ensemble dimension and
68 attempt to reconstruct the eddy flux of tracers defined as fluctuations about
69 the ensemble TWA mean. Unlike the spatiotemporal filtering approaches,
70 there is less ambiguity about how the eddy and mean are defined (Jamet
71 et al.), but the connection to parametrization in coarse-resolution models
72 still remains tenuous. Nonetheless, in this study we examine the eddy-mean
73 flow problem under this framework, which relatively novel in the ocean tur-
74 bulence literature. We also note that because the ensemble dimension is
75 orthogonal to the spatiotemporal dimensions, our Reynold’s decomposition

76 is exact. Our approach can be rephrased as us having the lofty long-term
77 goal to parametrize the oceanic intrinsic variability.

78 The paper is organized as follows: We describe the ensemble model con-
79 figurations and framework of the anisotropic eddy diffusivity tensor in Sec-
80 tion 2. The results are given in Section 3 with a discussion on the structural
81 similarity in eddy diffusivities that emerge between the two ensembles. We
82 conclude and provide some cautionary notes in Section 4.

83 2. Methods

84 Here we describe the quasi-geostrophic (QG) and realistic North Atlantic
85 (NA) ensembles, and then provide a brief description of the eddy diffusivity
86 tensor.

87 2.1. Quasi-geostrophic ensemble

88 The model outputs used here are those of Uchida et al. (2021b). For
89 completeness, we provide a brief overview of the configuration here. We use
90 the QG configuration of the Multiple Scale Ocean Model (MSOM; Deremble
91 and Martinez, 2020, hereon referred to as MSQG), based on the Basilisk
92 language (Popinet, 2015), to simulate a three-layer double-gyre flow with
93 a rigid lid and flat bottom. The characteristic length scale of the Rossby
94 radius is prescribed as 50 km and horizontal resolution is ~ 4 km, so we have
95 roughly 12 grid points per radius; our simulation can be considered mesoscale
96 resolving (Hallberg, 2013).

97 The model was forced with a stationary wind stress curl without any
98 buoyancy forcing at the surface. A seasonally varying background stratifica-
99 tion was prescribed at the first interface but kept stationary at the second
100 interface, which is consistent with the seasonal variability of stratification
101 being confined in the upper few hundred meters in the real ocean (Chelton
102 et al., 1998). The 101 ensemble members are initialized with stream func-
103 tions slightly perturbed at a single grid point randomly selected in the first
104 layer per member and the surface wind stress and temporally varying back-
105 ground stratification are kept identical amongst the members. We refer the
106 interested reader to Uchida et al. (2021b) for further details on the model
107 configuration and ensemble generation.

108 In addition, we added four passive tracers to each ensemble member with
109 the governing equation:

$$110 \quad C_{it} + J(\psi, C_i) = -\mathcal{F}^{-1}(C_i - \dot{C}_i), \quad (1)$$

111 where $C_i, i = 0, 1, 2, 3$ are the four passive tracers and ψ the stream function.
 112 They are relaxed towards a profile orthogonal to each other

$$113 \quad \dot{C}_0 = \frac{x - L/2}{L/2}, \quad \dot{C}_1 = \frac{y - L/2}{L/2}, \quad \dot{C}_2 = \sin \frac{2\pi x}{L}, \quad \dot{C}_3 = \sin \frac{2\pi y}{L}, \quad (2)$$

114 with a relaxation time scale of $\mathcal{T} \sim 360$ days for all three vertical layers.
 115 $L (= 4000 \text{ km})$ is the zonal and meridional domain extent, $x = [0, L], y =$
 116 $[0, L]$, resulting in the tracers taking values between $[-1, 1]$. The time scale
 117 chosen is similar to previous studies (e.g. Bachman et al., 2020), and meant
 118 to be longer than the typical eddy turn over time scale. In other words, the
 119 tracers are passively stirred by the flow realized by the intrinsic variability
 120 of each ensemble member but are relaxed towards identical profiles amongst
 121 members, the relaxation avoids the tracers from homogenizing (i.e. $\nabla_{\text{h}} C_i \neq \mathbf{0}$
 122 where ∇_{h} is the horizontal gradient operator).

123 The eddy flux $\mathbf{J}^C = \overline{u' C'} \mathbf{i} + \overline{v' C'} \mathbf{j}$ and mean tracer gradient $\nabla_{\text{h}} \overline{C}$ fields
 124 were further coarse grained by 4×4 grid-point boxcar filter in order to
 125 reduce the computational cost of inverting (5). \mathbf{i}, \mathbf{j} are the horizontal unit
 126 vectors in geopotential coordinates, and (\cdot) is the ensemble mean operator
 127 and $(\cdot)' \stackrel{\text{def}}{=} (\cdot) - \overline{(\cdot)}$.

128 *2.2. Realistic North Atlantic ensemble*

129 We use the model outputs from the realistic simulations described in
 130 Jamet et al. (2019, 2020), and Uchida et al. (2022b), which are 48 air-sea
 131 partially coupled ensemble members of the NA ocean at mesoscale-permitting
 132 resolution ($1/12^\circ$) using the hydrostatic configuration of the Massachusetts
 133 Institute of Technology general circulation model (MITgcm; Marshall et al.,
 134 1997). The modelled domain was configured to wrap around zonally in order
 135 to reduce memory allocation in running the simulation. Similar to the QG
 136 ensemble, in the latter subset of 24 members, four passive tracers per member
 137 were added using the RBCS package with the relaxation profiles of

$$138 \quad \dot{C}_0 = \frac{y - L^y/2}{L^y/2}; \quad \dot{C}_1 = \sin \frac{2\pi x}{L^x}; \quad \dot{C}_2 = \frac{z - H/2}{H/2}; \quad \dot{C}_3 = \sin \frac{2\pi y}{L^y}, \quad (3)$$

139 and the relaxation time scale of $\mathcal{T} = 365$ days. L^x, L^y are the zonal and
 140 meridional domain extent respectively and H is the deepest depth in the
 141 domain bathymetry.

142 The connection between primitive equations viewed in the thickness-
 143 weighted averaged (TWA) framework and quasi geostrophy is that in the
 144 latter, the layer thickness $\sigma \stackrel{\text{def}}{=} \zeta_{\bar{b}}$ only fluctuates on the order of Rossby
 145 number (ζ is the depth of the neutral surface and the subscript $\bar{(\cdot)}$ denotes
 146 derivatives in density coordinates). Hence, it can be argued that QG vari-
 147 ables are implicitly TWA and that for a fair comparison, the primitive equa-
 148 tions should also be TWA (cf. Marshall et al., 2012). The three-dimensional
 149 oceanic motions become quasi two dimensional upon thickness-weighted av-
 150 eraging (Aoki, 2014), further elucidating the similarity to quasi geostrophy.
 151 We proceed in defining our eddy tracer fluxes within the TWA framework,
 152 which gives $\mathbf{J}^C = J^{C1}\bar{\mathbf{e}}_1 + J^{C2}\bar{\mathbf{e}}_2 \stackrel{\text{def}}{=} \widehat{u''C''}\bar{\mathbf{e}}_1 + \widehat{v''C''}\bar{\mathbf{e}}_2$ where $\widehat{(\cdot)} \stackrel{\text{def}}{=} \bar{\sigma}^{-1}\overline{\sigma(\cdot)}$
 153 and $(\cdot)'' \stackrel{\text{def}}{=} (\cdot) - \widehat{(\cdot)}$ (Young, 2012). $\bar{\mathbf{e}}_1$ and $\bar{\mathbf{e}}_2$ are the horizontal unit vectors
 154 along the neutral surface. We note that due to the 3rd order direct-space-
 155 time (DST) flux-limiter advective scheme used, there are two possible ways
 156 to define the eddy flux, i.e. $\widehat{\mathbf{u}''C''} \approx \bar{\sigma}^{-1}(\overline{\sigma\mathbf{F}^C}) - \widehat{\mathbf{u}C}$ where \mathbf{F}^C is the DST
 157 advective flux computed by MITgcm. The advective scheme was chosen
 158 to be consistent with the schemes used for temperature and salinity. De-
 159 tails regarding the coordinate remapping from geopotential to approximately
 160 neutral density surfaces using the `xgcm` Python package (Abernathey et al.,
 161 2021), and the averaging are given in Uchida et al. (2022b).

162 As we do not expect the linear model (5) to capture grid-scale features,
 163 we first spatially smoothed the eddy flux and mean tracer fields by applying a
 164 Gaussian kernel with the standard deviation of 50 km using the `gcm-filters`
 165 Python package (Grooms et al., 2021). The eddy flux and mean tracer gradi-
 166 ent fields were then further coarse grained by 10×10 grid-point boxcar filter
 167 in order to capture the statistical properties of the eddies and reduce the
 168 computational cost of inversion. Each row in \mathbf{J} and \mathbf{G} was then normalized
 169 by horizontal median of the magnitude of each mean tracer gradient flux (i.e.
 170 $\frac{(\mathbf{J}^{C_i}, \mathbf{G}^{C_i})}{\text{median}[|\mathbf{G}^{C_i}|]}$ where \mathbf{J}^{C_i} and \mathbf{G}^{C_i} are the smoothed and coarse-grained eddy flux
 171 and mean gradient flux of an arbitrary tracer C_i) prior to the inversion so
 172 that each tracer had roughly equal weighting in inverting equation (5).

173 2.3. Eddy diffusivity tensor

174 As the eddy flux of tracers is generally poorly resolved in global forced and
 175 coupled ocean simulations, there has been an effort to parametrize this flux
 176 in the quasi-adiabatic interior via a local-gradient based model along neutral

177 surfaces (Redi, 1982; Griffies, 2004; Wilson and Williams, 2006; Holmes et al.,
 178 2022)

$$179 \quad \mathbf{J}^C = -\kappa \nabla_{\mathbf{h}} \bar{C}, \quad (4)$$

180 where κ is the scalar eddy diffusivity.

181 While it is tempting to directly infer a scalar eddy diffusivity from equa-
 182 tion (4), assuming an isotropic diffusivity for an anisotropic flow in realistic
 183 simulations is a poor approximation (Smith and Gent, 2004; Ferrari and
 184 Nikurashin, 2010; Fox-Kemper et al., 2013; Kamenkovich et al., 2020). A
 185 more appropriate model might be to relate the eddy fluxes to the mean gra-
 186 dients via a diffusivity tensor with four parameters (Plumb and Mahlman,
 187 1987), which has some justification in linear wave theories and mixing-length
 188 based models (Bachman and Fox-Kemper, 2013). In both these models, the
 189 inherent assumption is that the scalar diffusivity or diffusivity tensor is only
 190 a function of the flow, and is tracer independent.

191 We, therefore, take the approach of estimating the eddy diffusivity tensor
 192 (\mathbf{K}) from a least-squares best fit to (Plumb and Mahlman, 1987; Abernathey
 193 et al., 2013; Bachman and Fox-Kemper, 2013)

$$194 \quad \underbrace{\begin{pmatrix} J^{C_01} & J^{C_02} \\ J^{C_11} & J^{C_12} \\ J^{C_21} & J^{C_22} \\ J^{C_31} & J^{C_32} \end{pmatrix}}_{\mathbf{J}} = \mathbf{G} \cdot \underbrace{\begin{pmatrix} \kappa^{uu} & \kappa^{vu} \\ \kappa^{uv} & \kappa^{vv} \end{pmatrix}}_{\mathbf{K}}, \quad (5)$$

195 where for the QG ensemble

$$196 \quad \mathbf{G} = - \begin{pmatrix} \overline{C_{0x}} & \overline{C_{0y}} \\ \overline{C_{1x}} & \overline{C_{1y}} \\ \overline{C_{2x}} & \overline{C_{2y}} \\ \overline{C_{3x}} & \overline{C_{3y}} \end{pmatrix}, \quad (6)$$

197 and

$$198 \quad \mathbf{G} = - \begin{pmatrix} \widehat{C_{0\tilde{x}}} & \widehat{C_{0\tilde{y}}} \\ \widehat{C_{1\tilde{x}}} & \widehat{C_{1\tilde{y}}} \\ \widehat{C_{2\tilde{x}}} & \widehat{C_{2\tilde{y}}} \\ \widehat{C_{3\tilde{x}}} & \widehat{C_{3\tilde{y}}} \end{pmatrix}, \quad (7)$$

199 for the realistic NA ensemble respectively.

200 The least-squares fit can be estimated as $\mathbf{K} = \mathbf{G}^+\mathbf{J}$ where \mathbf{G}^+ is the Moore-
 201 Penrose pseudo inverse of \mathbf{G} for each data point (Bachman et al., 2015). It
 202 is possible to invert equation (5) with just two tracers whose gradients are
 203 not aligned with each other, and this will return a unique solution specific to
 204 the pair of tracers chosen for the inversion (e.g. Haigh and Berloff, 2021; Sun
 205 et al., 2021). Here, we instead focus on estimating a single tensor that works
 206 for all possible tracer orientations, even if it does not perfectly reconstruct
 207 the eddy flux for any single tracer. We have, thus, kept the system over-
 208 determined by using four tracers. The assumption is that by keeping it over
 209 determined, \mathbf{K} would extract the universal component in the relation between
 210 eddy fluxes and gradient flux of the mean tracer fields. From a practical point
 211 of view, all tracers should be associated with the same diffusivities in order
 212 to reduce the number of model parameters.

213 3. Results

214 We present results using the first time step of the fifth year, a time when
 215 the ensemble spread has converged for both ensembles (Uchida et al., 2022c;
 216 Jamet et al., 2019). The QG outputs are instantaneous snapshots while the
 217 North Atlantic (NA) outputs are five-day averaged.

218 3.1. Quasi-geostrophic ensemble

219 The four components in the eddy diffusivity tensor are provided in the top
 220 two rows of Fig. 1 with values reaching up to $O(10^4 \text{ m}^2 \text{ s}^{-1})$ in the first and
 221 second layer. The bottom layer is quiescent with diffusivities on the order of
 222 $O(10^2 \text{ m}^2 \text{ s}^{-1})$. The diagonal components of the tensor tend to take positive
 223 values over the entire domain while the antidiagonal components tend to
 224 change signs across the jet centered around $y = 2000 \text{ km}$. This suggests that
 225 the eddies are broadly working to dissipate small-scale variance, as one might
 226 expect. Focusing on the first layer, κ^{uv} tends to be coherently negative south
 227 of the jet and positive north of the jet. In the lower two layers, κ^{uv} and κ^{vu}
 228 tend to mirror each other where there is a sign change across the jet but also
 229 within each idealized subtropical and subpolar gyre. These cross diagonal
 230 terms of the tensor are largely associated with eddy-induced advection, and
 231 often act to oppose the mean flow (Marshall, 2011).

232 Taking the diagnosed tensor, we examine the reconstruction of the eddy
 233 flux of C_2 , i.e. $\mathbf{J}_{\text{reconstructed}}^{C_2} \stackrel{\text{def}}{=} -\nabla_h \overline{C_2} \cdot \mathbf{K}$. The middle two rows of Fig. 1 show
 234 that the performance of reconstruction is good across all three layers. The

Table 1: Spatial correlation for the four passive tracers and QGPV between the eddy flux and its reconstruction for the zonal and meridional orientation and all three layers. The PV coefficients are not shown for the middle and bottom layer as it is evident from Fig. 1 that the flux and reconstruction are completely decorrelated.

Tracer	Top	Middle	Bottom
r^{C_01}	0.952	0.989	0.999
r^{C_02}	0.957	0.990	0.996
r^{C_11}	0.980	0.966	0.981
r^{C_12}	0.999	0.999	0.997
r^{C_21}	0.939	0.978	0.993
r^{C_22}	0.949	0.966	0.973
r^{C_31}	0.992	0.969	0.980
r^{C_32}	0.999	0.999	0.997
r^{q1}	0.844	–	–
r^{q2}	0.906	–	–

235 spatial correlations between the actual eddy flux and its reconstruction are
 236 higher than 0.9 for all four tracers (Table 1). The spatial correlation was
 237 computed as

$$238 \quad r^{C_{ij}} = \frac{\sum \left[\left(J_{\text{true}}^{C_{ij}} - \langle J_{\text{true}}^{C_{ij}} \rangle \right) \left(J_{\text{reconstructed}}^{C_{ij}} - \langle J_{\text{reconstructed}}^{C_{ij}} \rangle \right) \right]}{\sqrt{\sum \left(J_{\text{true}}^{C_{ij}} - \langle J_{\text{true}}^{C_{ij}} \rangle \right)^2} \sqrt{\sum \left(J_{\text{reconstructed}}^{C_{ij}} - \langle J_{\text{reconstructed}}^{C_{ij}} \rangle \right)^2}}, \quad (8)$$

239 where $\langle \cdot \rangle$ is the horizontal spatial mean, $j = 1, 2$ correspond to the zonal and
 240 meridional orientation, and the summation is taken over the entire domain
 241 of interest.

242 As the inversion was done as a least squares fit to (5), the good recon-
 243 struction of \mathbf{J}^C may not come as a surprise and is consistent with previous
 244 studies (e.g. Abernathey et al., 2013; Bachman et al., 2015, 2020). However,
 245 it is important to note that such a good fit suggests that the diffusion ten-
 246 sor model with four free parameters is a good model to represent how the
 247 eddies flux different tracers along neutral surfaces. This model is able to
 248 separate the contribution of the flow from any dependence on the orienta-
 249 tion of tracer gradients well, and this model of reduced complexity can be a
 250 target for parametrizations that are able to represent the eddy fluxes of any
 251 arbitrary passive tracer.

252 One may now ask the question: Can the tensor diagnosed from passive
 253 tracers be applied to active tracers, here chosen as QG potential vorticity
 254 (PV), which is the sole active tracer in quasi geostrophy? Looking at the
 255 bottom two rows of Fig. 1, we see that while the reconstruction $-\nabla_{\text{h}}\bar{q} \cdot \mathbf{K}$
 256 captures some features in the top layer (cf. Table 1) and in the regions away
 257 from the jet in the middle layer, the reconstruction performs poorly for the
 258 bottom layers and in the jet in the middle layer, with the spatial correlations
 259 being smaller than 0.1.

260 3.2. Realistic North Atlantic ensemble

261 Following the QG analyses, we now present the four components of the
 262 tensor \mathbf{K} from the NA ensemble. The magnitude of the tensor components
 263 are similar to the QG ensemble, reaching up to $O(10^4 \text{ m}^2 \text{ s}^{-1})$ (top left four
 264 panels in Fig. 2). Also similar to the QG ensemble, the diagonal compo-
 265 nents tend to take positive values while the antidiagonal components tend
 266 to change signs across the separated Gulf Stream (GS). The separated GS
 267 can be identified in the top right panel in Fig. 2 where the ensemble-mean
 268 depth associated with the neutral surface shoals around 35°N . We also show
 269 the vertical transects along 300°E . The patterns in sign persist over depth
 270 with the order of magnitude decreasing towards $O(10^2 \text{ m}^2 \text{ s}^{-1})$ in the abyssal
 271 ocean (bottom four panels in Fig. 2).

272 We remind the reader that we define the eddy flux as $\mathbf{J}^C \stackrel{\text{def}}{=} \widehat{\mathbf{u}''C''}$, and
 273 following the convention of the TWA framework, the reconstructed eddy flux
 274 of C_1 becomes $\mathbf{J}_{\text{reconstructed}}^{C_1} \stackrel{\text{def}}{=} -\widetilde{\nabla}_{\text{h}}\widehat{C_1} \cdot \mathbf{K}$. In examining the reconstruction,
 275 we limit it to regions where the neutral surface is deeper than 150 m and
 276 to grids upon the 10×10 coarse graining included no land cells in order to
 277 minimize the effect of diabatic mixing (here parametrized by the K-Profile
 278 Parametrization; Large et al., 1994). As we see from Fig. 3, the recon-
 279 struction of eddy passive tracer fluxes is good generally across the entire
 280 three dimensional domain (Table 2). The largest disagreements between \mathbf{J}^{C_i}
 281 and $\mathbf{J}_{\text{reconstructed}}^{C_i}$ can be seen in the separated GS region where eddy activity
 282 and vertical fluctuations of the neutral surface are vigorous (Uchida et al.,
 283 2022b). The horizontal spatial correlation improves for the quiescent gyre
 284 interior with values higher than 0.9 for all four passive tracers.

285 We may now also examine if we can use the tensor to reconstruct the
 286 eddy temperature and salinity fluxes, variables which were not included in
 287 the inversion of (5) and are active tracers. Overall the level of reconstruction

Table 2: Spatial correlation for the four passive tracers and temperature and salinity between the eddy flux and its reconstruction for the zonal and meridional orientation along the neutral surface shown in Fig. 2. The correlation coefficients are shown for when they are diagnosed over the entire horizontal domain and only between 10°N-30°N both excluding the hatched regions in Figs. 3 and 4.

Tracer	Entire domain	10°N-30°N
r^{C_01}	0.698	0.946
r^{C_02}	0.784	0.958
r^{C_11}	0.894	0.965
r^{C_12}	0.838	0.941
r^{C_21}	0.991	0.963
r^{C_22}	0.994	0.981
r^{C_31}	0.794	0.944
r^{C_32}	0.901	0.959
$r^{\Theta 1}$	0.303	0.539
$r^{\Theta 2}$	0.346	0.547
r^{S1}	0.102	0.098
r^{S2}	0.130	0.086

288 is poorer than that of passive tracers particularly in the separated GS region;
 289 the discrepancy north of 30°N extends vertically down to ~ 1000 m (bottom
 290 two rows in Fig. 4). It is interesting, however, that there seems to be some
 291 utility of the tensor in the quiescent gyre interior, particularly for tempera-
 292 ture (top three rows of Fig. 4, Table 2); $\mathbf{J}_{\text{reconstructed}}^{\Theta}$ and $\mathbf{J}_{\text{reconstructed}}^S$ capture
 293 the sign structure south of 30°N in \mathbf{J}^{Θ} and \mathbf{J}^S respectively. Given the QGPV
 294 results from the previous section, we did not attempt the reconstruction for
 295 Ertel’s PV.

296 4. Conclusion and discussion

297 In this study, we have diagnosed the mesoscale eddy diffusivity tensor
 298 \mathbf{K} using passive tracer outputs from two sets of ensemble simulations: an
 299 idealized 101-member quasi-geostrophic (QG) double-gyre ensemble and a
 300 realistic 24-member ensemble of the North Atlantic (NA). In decomposing the
 301 eddies and mean flow, we have chosen to take the averaging operator over
 302 the ensemble dimension rather than the often employed spatial or temporal
 303 dimension (e.g. Balwada et al., 2020; Bachman et al., 2020; Kamenkovich
 304 et al., 2020; Haigh and Berloff, 2021) with the aim of capturing the intrinsic

305 variability of eddy transport. We have also investigated the tensor in the
 306 thickness-weighted averaged (TWA) context, which to our knowledge, is the
 307 first study to do so. While we have only utilized one time slice of output, we
 308 do not expect the performance of inverting for \mathbf{K} to qualitatively vary over
 309 time in the quasi-adiabatic interior of the ocean.

310 The diagnosed tensor shows good performance in reconstructing the eddy
 311 fluxes of passive tracers from the gradient flux of mean passive tracer fields,
 312 which were weakly restored with a one-year relaxation timescale. The agree-
 313 ment between the spatial patterns in the diffusivities emerging from the QG
 314 and NA ensemble in respect to the position of the jet is also comforting; they
 315 have similar orders of magnitude and the diagonal components (κ_{uu}, κ_{vv}) tend
 316 to be positive while κ_{uv}, κ_{vu} tend to have opposite signs across the jet and
 317 change signs within each gyre. This partially justifies our assumption that
 318 there is a universal eddy diffusivity tensor, which is able to represent the eddy
 319 flux across passive tracers. As noted in Section 2.2, there are two possible
 320 ways to define the eddy tracer fluxes as soon as the advective scheme becomes
 321 more complicated than a 2nd-order centered scheme. We also diagnosed the
 322 tensor with the eddy fluxes defined as $\mathbf{J}^C \stackrel{\text{def}}{=} \bar{\sigma}^{-1}(\overline{\sigma \mathbf{F}^C}) - \hat{\mathbf{u}}\hat{C}$ but the per-
 323 formance of reconstruction deteriorated compared to when $\mathbf{J}^C \stackrel{\text{def}}{=} \widehat{\mathbf{u}''C''}$ (not
 324 shown). We speculate that the linear gradient flux model (5) is unable to
 325 capture the non-linearities in the flux-limiter advective scheme used in our
 326 simulations for all passive and active tracers.

327 Given the diagnosed diffusivity tensor from passive tracers, we have fur-
 328 ther examined whether it can be carried over to inform the parametrization
 329 of active tracer fluxes. However, when applying the tensor to reconstruct the
 330 eddy fluxes of active tracers, here QG potential vorticity (PV), our results
 331 suggest that passive and active tracers have significantly different eddy dif-
 332 fusivities. In other words, passive and active tracers have different relations
 333 between the eddy fluxes and mean fields and this likely stems from the fact
 334 that for QGPV, there is no restoring force as in what we prescribed for the
 335 passive tracers particularly below the first layer. We note that without any
 336 restoring for passive tracers, their concentrations would completely homoge-
 337 nize over time ($\nabla_{\mathbf{h}} C_i = \mathbf{0}$) rendering the gradient flux model (5) useless. Our
 338 emphasis on the eddy PV flux is because it encapsulates the energy backscat-
 339 tering onto the mean flow (Young, 2012; Marshall et al., 2012; Uchida et al.,
 340 2021a). Machine learning methods or further generalizations to the frame-
 341 work may provide a pathway forward in finding the relation for active tracers

342 (e.g. Zanna and Bolton, 2020; Frezat et al., 2021; Lu et al., 2022).

343 Nonetheless, the development of a prognostic and physically consistent \mathbf{K}
344 will likely benefit biogeochemical modelling since biogeochemical tracers are
345 passive (cf. Jones and Abernathey, 2019; Uchida et al., 2020). We end on
346 the note that for the realistic NA ensemble, the tensor shows some skill in
347 reconstructing the eddy temperature and salinity fluxes in the gyre interior.
348 While temperature and salinity are not purely passive as they affect the
349 dynamics via the hydrostatic pressure, the partial reconstruction may suggest
350 that they have less of a direct role on the dynamics compared to PV.

351 **Data availability statement**

352 The Jupyter notebooks used for the analyses of the QG and North At-
353 lantic ensembles are available via Github ([https://github.com/roxyboy/
354 Dahu_ML](https://github.com/roxyboy/Dahu_ML) and <https://github.com/roxyboy/TWA-eddy-diffusivity> respec-
355 tively; DOIs will be added upon acceptance of the manuscript).

356 **Declaration of competing interest**

357 The authors declare no conflict of interest.

358 **Acknowledgements**

359 This study is a contribution to the ‘Assessing the Role of forced and
360 internal Variability for the Ocean and climate Response in a changing cli-
361 mate’ (ARVOR) project supported by the French ‘Les Enveloppes Fluides
362 et l’Environnement’ (LEFE) program. This work was supported via Na-
363 tional Science Foundation (NSF) grants OCE-1829856, OCE-2023585, OCE-
364 2123632 and the French ‘Make Our Planet Great Again’ (MOPGA) program
365 managed by the Agence Nationale de la Recherche under the Programme
366 d’Investissement d’Avenir, reference ANR-18-MPGA-0002. The latter grant
367 served as the primary support for Uchida and partially for Jamet. Bal-
368 wada acknowledges support from the NSF grant OCE-1756882. We ac-
369 knowledge high-performance computing resources for generating the QG en-
370 semble on Occigen, which was maintained by CINES with the reference
371 A0090112020. The open-source software for MSOM can be found at [github.
372 com/bderembl/msom](https://github.com/bderembl/msom). It was developed as a module of Basilisk (available at
373 basilisk.fr). High-performance computing resources on Cheyenne (doi:

374 10.5065/D6RX99HX) used for running the NA ensembles were provided by
375 NCAR’s Computational and Information Systems Laboratory, sponsored by
376 NSF, under the university large allocation UFSU0011. Uchida personally
377 thanks the Oceanography with an Alpine Flair workshop held in Grenoble
378 2022, which has led to fruitful exchanges. The model diagnostics were exe-
379 cuted on the Florida State University and Université Grenoble Alpes clusters.

380 References

381 Abernathey, R.P., Busecke, J., Smith, T., Banihirwe, A., Fernandes, F.,
382 Bourbeau, J., Cherian, D., Dussin, R., Swanson-Hysell, N., Constantinou,
383 N., Ponte, A., et al., 2021. *xgcm*: General circulation model postprocessing
384 with xarray. URL: <https://xgcm.readthedocs.io/en/latest/>, doi:10.
385 5281/zenodo.3634752.

386 Abernathey, R.P., Ferreira, D., Klocker, A., 2013. Diagnostics of isopycnal
387 mixing in a circumpolar channel. *Ocean Modelling* 72, 1–16. doi:10.1016/
388 j.ocemod.2013.07.004.

389 Aiki, H., Richards, K.J., 2008. Energetics of the global ocean: The role of
390 layer-thickness form drag. *Journal of Physical Oceanography* 38, 1845–
391 1869. doi:10.1175/2008JP03820.1.

392 Aoki, K., 2014. A constraint on the thickness-weighted average equation of
393 motion deduced from energetics. *Journal of Marine Research* 72, 355–382.
394 doi:10.1357/002224014815469886.

395 Bachman, S.D., 2019. The GM+E closure: A framework for coupling
396 backscatter with the Gent and McWilliams parameterization. *Ocean Mod-
397 elling* 136, 85–106. doi:10.1016/j.ocemod.2019.02.006.

398 Bachman, S.D., Fox-Kemper, B., 2013. Eddy parameterization challenge
399 suite I: Eady spindown. *Ocean Modelling* 64, 12–28. doi:10.1016/j.
400 ocemod.2012.12.003.

401 Bachman, S.D., Fox-Kemper, B., Bryan, F.O., 2015. A tracer-based inver-
402 sion method for diagnosing eddy-induced diffusivity and advection. *Ocean
403 Modelling* 86, 1–14. doi:10.1016/j.ocemod.2014.11.006.

- 404 Bachman, S.D., Fox-Kemper, B., Bryan, F.O., 2020. A diagnosis of
405 anisotropic eddy diffusion from a high-resolution global ocean model.
406 Journal of Advances in Modeling Earth Systems 12, e2019MS001904.
407 doi:10.1029/2019MS001904.
- 408 Balwada, D., Smith, K.S., Abernathey, R.P., 2020. Measuring eddy driven
409 transport in a zonally inhomogeneous flow, in: Ocean Sciences Meeting
410 2020, AGU.
- 411 Chang, P., Zhang, S., Danabasoglu, G., Yeager, S.G., Fu, H., Wang, H.,
412 Castruccio, F.S., Chen, Y., Edwards, J., Fu, D., et al., 2020. An unprece-
413 dented set of high-resolution earth system simulations for understanding
414 multiscale interactions in climate variability and change. Journal of Ad-
415 vances in Modeling Earth Systems 12, e2020MS002298.
- 416 Chassignet, E.P., Xu, X., 2021. On the importance of high-resolution in
417 large-scale ocean models. Advances in Atmospheric Sciences , 1–14doi:10.
418 1007/s00376-021-0385-7.
- 419 Chassignet, E.P., Yeager, S.G., Fox-Kemper, B., Bozec, A., Castruccio, F.,
420 Danabasoglu, G., Horvat, C., Kim, W.M., Koldunov, N., Li, Y., et al.,
421 2020. Impact of horizontal resolution on global ocean–sea ice model simu-
422 lations based on the experimental protocols of the Ocean Model Intercom-
423 parison Project phase 2 (OMIP-2). Geoscientific Model Development 13,
424 4595–4637. doi:10.5194/gmd-13-4595-2020.
- 425 Chelton, D.B., DeSzoeki, R.A., Schlax, M.G., El Naggar, K., Siwertz, N.,
426 1998. Geographical variability of the first baroclinic rossby radius of de-
427 formation. Journal of Physical Oceanography 28, 433–460.
- 428 Deremble, B., Martinez, E.M., 2020. MSOM: Multiple Scale Ocean
429 Model. URL: <https://github.com/bderembl/msom>, doi:10.5281/
430 zenodo.4669909.
- 431 Eden, C., Greatbatch, R.J., 2008. Towards a mesoscale eddy closure. Ocean
432 Modelling 20, 223–239. doi:10.1016/j.ocemod.2007.09.002.
- 433 Fedele, G., Penduff, T., Pierini, S., Alvarez-Castro, M.C., Bellucci, A.,
434 Masina, S., 2021. Interannual to decadal variability of the Kuroshio exten-
435 sion: analyzing an ensemble of global hindcasts from a dynamical system
436 viewpoint. Climate Dynamics , 1–18doi:10.1007/s00382-021-05751-7.

- 437 Ferrari, R., Nikurashin, M., 2010. Suppression of eddy diffusivity across jets
438 in the Southern Ocean. *Journal of Physical Oceanography* 40, 1501–1519.
439 doi:10.1175/2010JP04278.1.
- 440 Fox-Kemper, B., Lumpkin, R., Bryan, F.O., 2013. Lateral transport in the
441 ocean interior, in: *International Geophysics*. Elsevier. volume 103, pp.
442 185–209.
- 443 Frezat, H., Balarac, G., Le Sommer, J., Fablet, R., Lguensat, R., 2021. Phys-
444 ical invariance in neural networks for subgrid-scale scalar flux modeling.
445 *Physical Review Fluids* 6, 024607.
- 446 Griffies, S.M., 2004. *Fundamentals of ocean climate models*. Princeton uni-
447 versity press.
- 448 Griffies, S.M., Winton, M., Anderson, W.G., Benson, R., Delworth, T.L.,
449 Dufour, C.O., Dunne, J.P., Goddard, P., Morrison, A.K., Rosati, A.,
450 et al., 2015. Impacts on ocean heat from transient mesoscale eddies
451 in a hierarchy of climate models. *Journal of Climate* 28, 952–977.
452 doi:10.1175/JCLI-D-14-00353.1.
- 453 Grooms, I., Loose, N., Abernathey, R., Steinberg, J., Bachman, S.D.,
454 Marques, G., Guillaumin, A.P., Yankovsky, E., 2021. Diffusion-based
455 smoothers for spatial filtering of gridded geophysical data. *Jour-
456 nal of Advances in Modeling Earth Systems* , e2021MS002552URL:
457 <https://gcm-filters.readthedocs.io/en/latest/>, doi:10.1029/
458 2021MS002552.
- 459 Guillaumin, A.P., Zanna, L., 2021. Stochastic-deep learning parameteriza-
460 tion of ocean momentum forcing. *Journal of Advances in Modeling Earth
461 Systems* 13, e2021MS002534.
- 462 Haigh, M., Berloff, P., 2021. On co-existing diffusive and anti-diffusive tracer
463 transport by oceanic mesoscale eddies. *Ocean Modelling* 168, 101909.
- 464 Hallberg, R., 2013. Using a resolution function to regulate parameterizations
465 of oceanic mesoscale eddy effects. *Ocean Modelling* 72, 92–103. doi:10.
466 1016/j.ocemod.2013.08.007.

- 467 Hewitt, H., Fox-Kemper, B., Pearson, B., Roberts, M., Klocke, D., 2022. The
468 small scales of the ocean may hold the key to surprises. *Nature Climate*
469 *Change* doi:10.1038/s41558-022-01386-6.
- 470 Holmes, R.M., Groeskamp, S., Stewart, K.D., McDougall, T.J., 2022. Sen-
471 sitivity of a coarse-resolution global ocean model to a spatially variable
472 neutral diffusivity. *Journal of Advances in Modeling Earth Systems* 14,
473 e2021MS002914.
- 474 Jamet, Q., Dewar, W.K., Wienders, N., Deremble, B., 2019. Spatiotemporal
475 Patterns of Chaos in the Atlantic Overturning Circulation. *Geophysical*
476 *Research Letters* 46, 7509–7517. doi:10.1029/2019GL082552.
- 477 Jamet, Q., Dewar, W.K., Wienders, N., Deremble, B., Close, S., Penduff, T.,
478 2020. Locally and remotely forced subtropical AMOC variability: A matter
479 of time scales. *Journal of Climate* doi:10.1175/JCLI-D-19-0844.1.
- 480 Jamet, Q., Leroux, S., Dewar, W.K., Penduff, T., Le Sommer, J., Mo-
481 lines, J.M., J, G., . Non-local eddy-mean kinetic energy transfers in
482 submesoscale-permitting ensemble simulations. *Journal of Advances in*
483 *Modeling Earth Systems* 14, e2022MS003057.
- 484 Jansen, M.F., Adcroft, A., Khani, S., Kong, H., 2019. Toward an ener-
485 getically consistent, resolution aware parameterization of ocean mesoscale
486 eddies. *Journal of Advances in Modeling Earth Systems* 11, 2844–2860.
487 doi:10.1029/2019MS001750.
- 488 Jones, S.C., Abernathey, R.P., 2019. Isopycnal mixing controls deep ocean
489 ventilation. *Geophysical Research Letters* doi:10.1029/2019GL085208.
- 490 Kamenkovich, I., Berloff, P., Haigh, M., Sun, L., Lu, Y., 2020. Complexity
491 of mesoscale eddy diffusivity in the ocean. *Geophysical Research Letters* ,
492 e2020GL091719doi:10.1029/2020GL091719.
- 493 Killworth, P.D., 1997. On the parameterization of eddy transfer Part
494 I. Theory. *Journal of Marine Research* 55, 1171–1197. doi:10.1357/
495 0022240973224102.
- 496 Large, W.G., McWilliams, J.C., Doney, S.C., 1994. Oceanic vertical mixing:
497 A review and a model with a nonlocal boundary layer parameterization.
498 *Reviews of geophysics* 32, 363–403. doi:10.1029/94rg01872.

- 499 Leroux, S., Penduff, T., Bessières, L., Molines, J.M., Brankart, J.M., Sérazin,
500 G., Barnier, B., Terray, L., 2018. Intrinsic and atmospherically forced
501 variability of the AMOC: insights from a large-ensemble ocean hindcast.
502 *Journal of Climate* 31, 1183–1203. doi:10.1175/JCLI-D-17-0168.1.
- 503 Lu, Y., Kamenkovich, I., Berloff, P., 2022. Properties of the lateral mesoscale
504 eddy-induced transport in a high-resolution ocean model: Beyond the
505 flux-gradient relation. *Journal of Physical Oceanography* doi:10.1175/
506 JPO-D-22-0108.1.
- 507 Marshall, D.P., Maddison, J.R., Berloff, P.S., 2012. A framework for parame-
508 terizing eddy potential vorticity fluxes. *Journal of Physical Oceanography*
509 42, 539–557. doi:10.1175/JPO-D-11-048.1.
- 510 Marshall, J., 2011. A pedagogical example of Eulerian and Lagrangian flows
511 induced by Rossby wave rectification in an ocean basin. *Journal of Marine*
512 *Research* 69, 647–657.
- 513 Marshall, J., Hill, C., Perelman, L., Adcroft, A., 1997. Hydrostatic, quasi-
514 hydrostatic, and nonhydrostatic ocean modeling. *Journal of Geophysical*
515 *Research: Oceans* 102, 5733–5752. URL: [https://mitgcm.readthedocs.](https://mitgcm.readthedocs.io/en/latest/)
516 [io/en/latest/](https://mitgcm.readthedocs.io/en/latest/), doi:10.1029/96JC02776.
- 517 Plumb, R., Mahlman, J., 1987. The zonally averaged transport characteris-
518 tics of the GFDL general circulation/transport model. *Journal of the atmo-*
519 *spheric sciences* 44, 298–327. doi:10.1175/1520-0469(1987)044<0298:
520 TZATCO>2.0.CO;2.
- 521 Popinet, S., 2015. A quadtree-adaptive multigrid solver for the Serre-Green-
522 Naghdi equations. *Journal of Computational Physics* 302, 336–358. doi:10.
523 1016/j.jcp.2015.09.009.
- 524 Redi, M.H., 1982. Oceanic isopycnal mixing by coordinate rotation. *Journal*
525 *of Physical Oceanography* 12, 1154–1158. doi:10.1175/1520-0485(1982)
526 012<1154:OIMBCR>2.0.CO;2.
- 527 Sérazin, G., Penduff, T., Barnier, B., Molines, J.M., Arbic, B.K., Müller, M.,
528 Terray, L., 2018. Inverse cascades of kinetic energy as a source of intrinsic
529 variability: A global OGCM study. *Journal of Physical Oceanography* 48,
530 1385–1408. doi:10.1175/JPO-D-17-0136.1.

- 531 Small, R.J., Bacmeister, J., Bailey, D., Baker, A., Bishop, S., Bryan, F.,
532 Caron, J., Dennis, J., Gent, P., Hsu, H.m., et al., 2014. A new synoptic
533 scale resolving global climate simulation using the Community Earth Sys-
534 tem Model. *Journal of Advances in Modeling Earth Systems* 6, 1065–1094.
- 535 Smith, R.D., Gent, P.R., 2004. Anisotropic Gent–McWilliams parameteriza-
536 tion for ocean models. *Journal of Physical Oceanography* 34, 2541–2564.
537 doi:10.1175/JP02613.1.
- 538 Sun, L., Haigh, M., Shevchenko, I., Berloff, P., Kamenkovich, I., 2021. On
539 non-uniqueness of the mesoscale eddy diffusivity. *Journal of Fluid Mechan-*
540 *ics* 920.
- 541 Uchida, T., Abernathey, R.P., Smith, K.S., 2017. Seasonality of eddy kinetic
542 energy in an eddy permitting global climate model. *Ocean Modelling* 118,
543 41–58. doi:10.1016/j.ocemod.2017.08.006.
- 544 Uchida, T., Balwada, D., Abernathey, R.P., McKinley, G.A., Smith, K.S.,
545 Lévy, M., 2019. The contribution of submesoscale over mesoscale eddy iron
546 transport in the open Southern Ocean. *Journal of Advances in Modeling*
547 *Earth Systems* 11, 3934–3958. doi:10.1029/2019MS001805.
- 548 Uchida, T., Balwada, D., Abernathey, R.P., McKinley, G.A., Smith, K.S.,
549 Lévy, M., 2020. Vertical eddy iron fluxes support primary production in
550 the open Southern Ocean. *Nature communications* 11, 1–8. doi:10.1038/
551 s41467-020-14955-0.
- 552 Uchida, T., Deremble, B., Dewar, W.K., Penduff, T.,
553 2021a. Diagnosing the Eliassen-Palm flux from a quasi-
554 geostrophic double gyre ensemble, in: *EarthCube Annual*
555 *Meeting, NSF*. URL: [https://earthcube2021.github.io/
556 ec21_book/notebooks/ec21_uchida_et al/notebooks/TU_05_
557 Diagnosing-the-Eliassen-Palm-flux-from-a-quasi-geostrophic-double-gyre-ensemble](https://earthcube2021.github.io/ec21_book/notebooks/ec21_uchida_et al/notebooks/TU_05_Diagnosing-the-Eliassen-Palm-flux-from-a-quasi-geostrophic-double-gyre-ensemble.html)
558 [html](https://earthcube2021.github.io/ec21_book/notebooks/ec21_uchida_et al/notebooks/TU_05_Diagnosing-the-Eliassen-Palm-flux-from-a-quasi-geostrophic-double-gyre-ensemble.html), doi:10.5281/zenodo.5496375.
- 559 Uchida, T., Deremble, B., Penduff, T., 2021b. The seasonal variability of the
560 ocean energy cycle from a quasi-geostrophic double gyre ensemble. *Fluids*
561 6, 206. doi:10.3390/fluids6060206.

- 562 Uchida, T., Deremble, B., Popinet, S., 2022a. Deterministic model of
563 the eddy dynamics for a midlatitude ocean model. *Journal of Physical*
564 *Oceanography* 52, 1133–1154.
- 565 Uchida, T., Jamet, Q., Dewar, W.K., Le Sommer, J., Penduff, T., Balwada,
566 D., 2022b. Diagnosing the thickness-weighted averaged eddy-mean flow
567 interaction from an eddying North Atlantic ensemble: The Eliassen-Palm
568 flux. *Journal of Advances in Modeling Earth Systems* 14, e2021MS002866.
569 doi:10.1029/2021MS002866.
- 570 Uchida, T., Le Sommer, J., Stern, C., Abernathey, R.P., Holdgraf, C., Al-
571 bert, A., Brodeau, L., Chassignet, E.P., Xu, X., Gula, J., et al., 2022c.
572 Cloud-based framework for inter-comparing submesoscale-permitting real-
573 istic ocean models. *Geoscientific Model Development* .
- 574 Vallis, G.K., 2017. *Atmospheric and oceanic fluid dynamics*. 2 ed., Cambridge
575 University Press.
- 576 Wilson, C., Williams, R.G., 2006. When are eddy tracer fluxes directed
577 downgradient? *Journal of Physical Oceanography* 36, 189–201. doi:10.
578 1175/JP02841.1.
- 579 Young, W.R., 2012. An exact thickness-weighted average formulation of
580 the boussinesq equations. *Journal of Physical Oceanography* 42, 692–707.
581 doi:10.1175/JP0-D-11-0102.1.
- 582 Zanna, L., Bolton, T., 2020. Data-driven equation discovery of ocean
583 mesoscale closures. *Geophysical Research Letters* , e2020GL088376doi:10.
584 1029/2020GL088376.

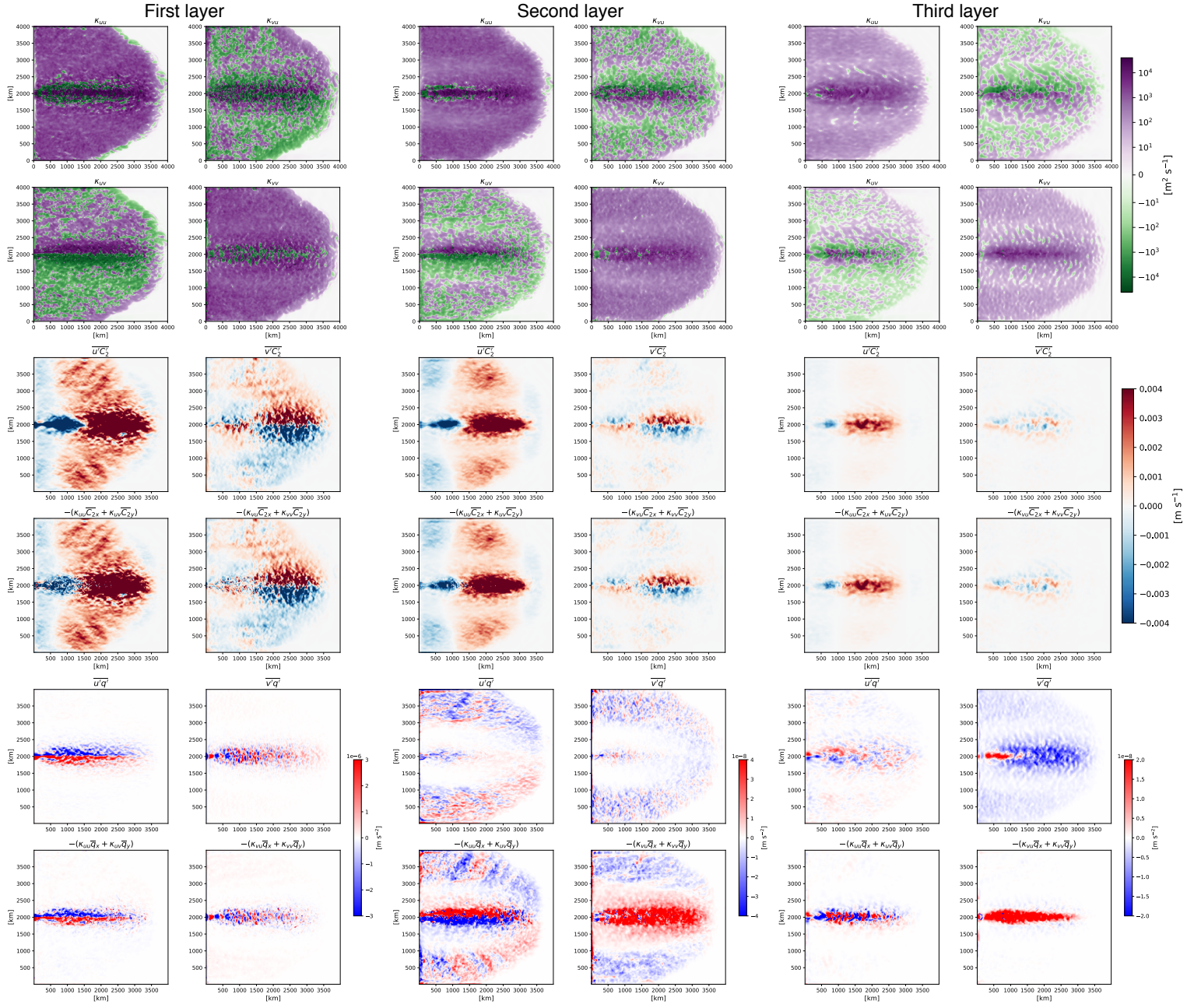


Figure 1: The eddy diffusivity tensor \mathbf{K} diagnosed by inverting (5), eddy flux of C_2 and PV and their reconstruction from the QG ensemble for all three layers. The four components of the tensor are exhibited in the top two rows, the eddy flux \mathbf{J}^{C_2} and its reconstruction $-\nabla_{\mathbf{h}} \overline{C_2} \cdot \mathbf{K}$ in the middle two rows, and the tensor applied to PV (q) in the bottom two rows. The eddy PV fluxes in the bottom two layers are two orders of magnitude smaller than the top layer.

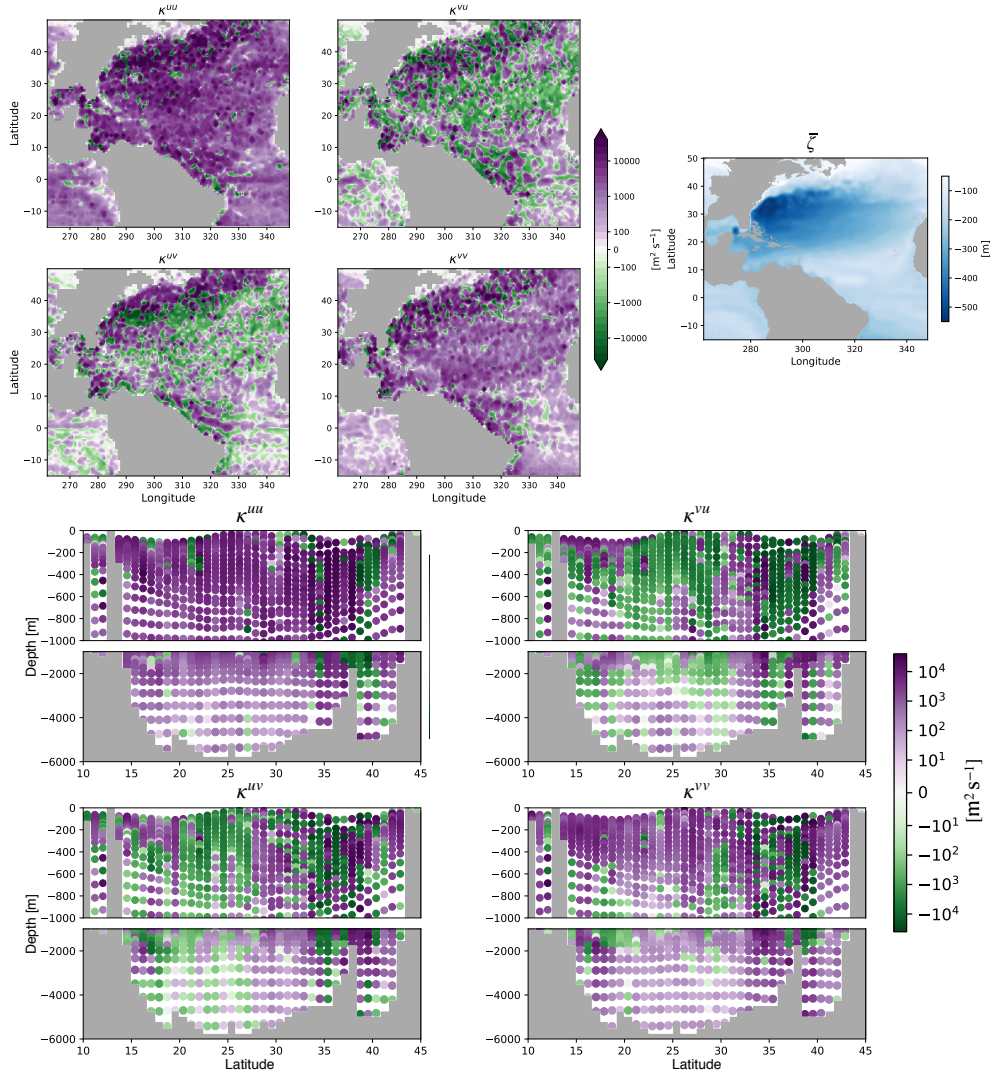


Figure 2: The eddy diffusivity tensor \mathbf{K} diagnosed by inverting (5) from the realistic North Atlantic ensemble on January 3, 1967. The top left four panels show the four components along the neutral surface associated with the ensemble-mean depth \bar{z} shown in the right top panel. The bottom four panels exhibit the vertical transect of the four components along 300°E .

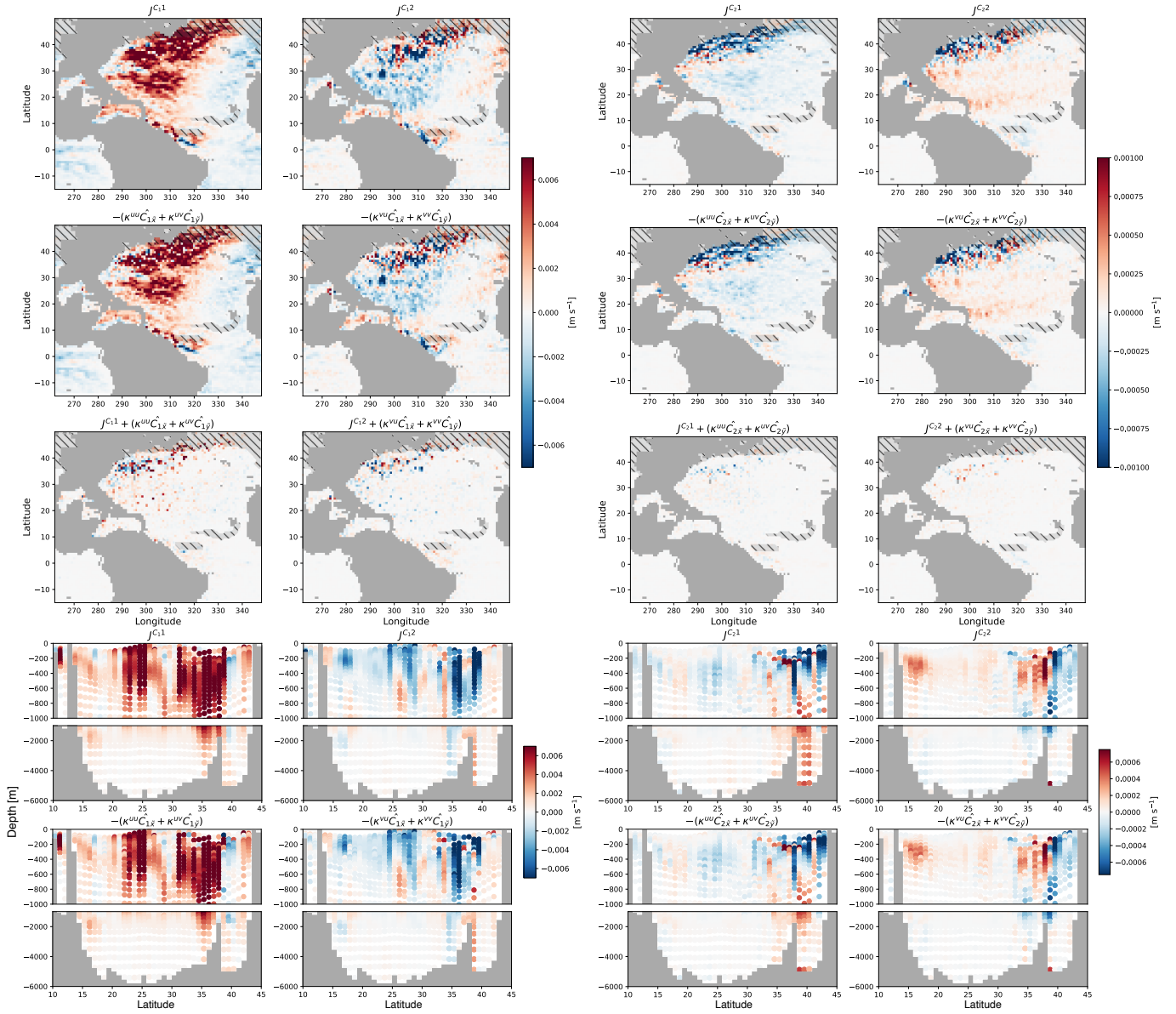


Figure 3: The eddy flux of tracers C_1 and C_2 and their reconstruction from the realistic North Atlantic ensemble on January 3, 1967. The top three rows present the eddy flux J^{C_i} , reconstruction $-\nabla_h \widehat{C}_i \cdot \mathbf{K}$, and the difference between the two respectively. The hatches indicate regions where the neutral surface is shallower than 150 m. The bottom two rows exhibit the vertical transect of the flux and reconstruction along 300°E .

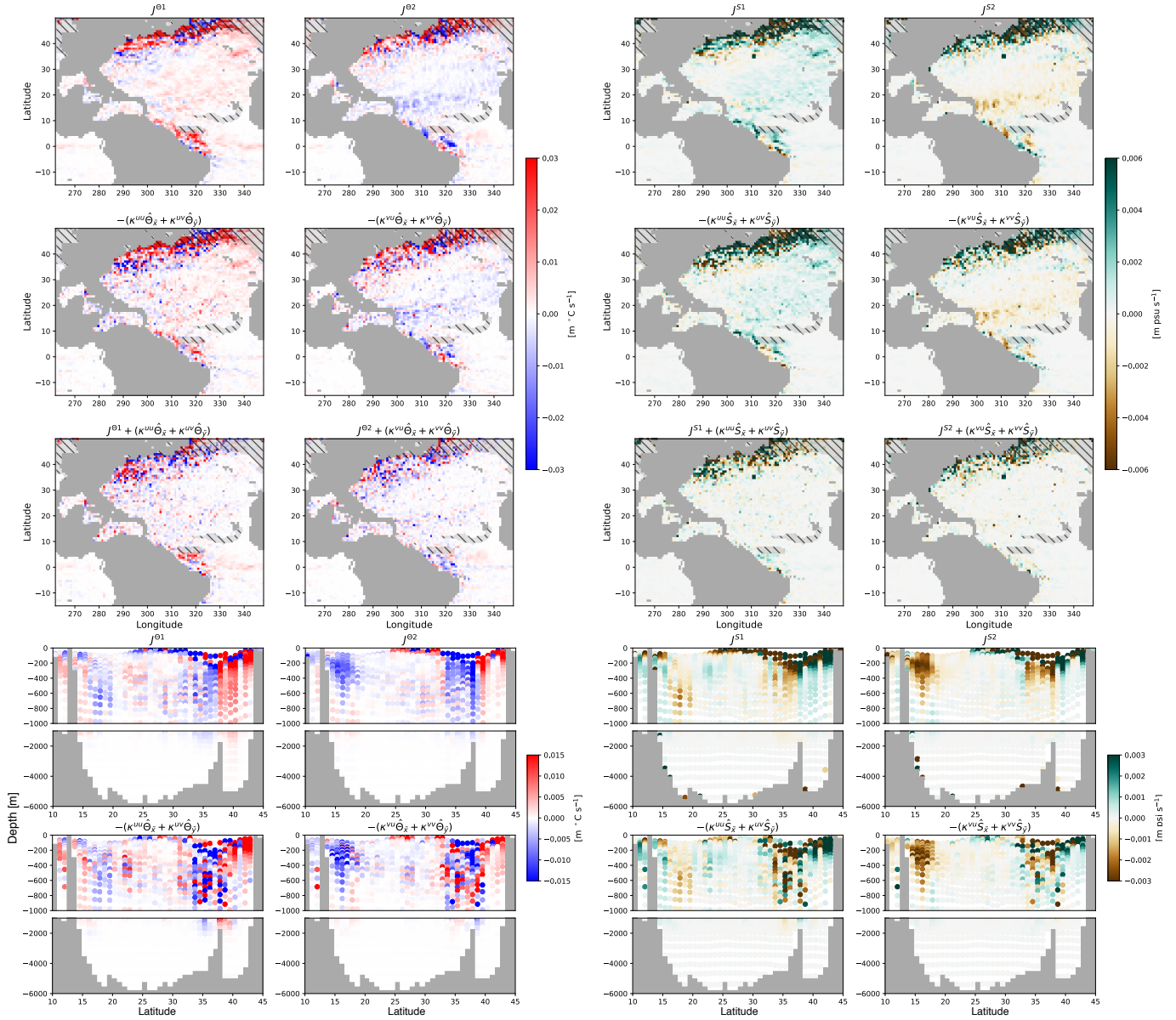


Figure 4: The eddy flux of potential temperature and practical salinity, and their reconstruction from the realistic North Atlantic ensemble on January 3, 1967. The top three rows present the eddy flux \mathbf{J}^Θ , \mathbf{J}^S , reconstruction $-\nabla_{\text{h}}(\hat{\Theta}, \hat{S}) \cdot \mathbf{K}$, and the difference between the two respectively. The hatches indicate regions where the neutral surface is shallower than 150 m. The bottom two rows exhibit the vertical transect of the flux and reconstruction along 300°E .